



A Powered Hip Exoskeleton With High Torque Density for Walking, Running, and Stair Ascent

Marshall K. Ishmael, Student Member, IEEE, Dante Archangeli, and Tommaso Lenzi, Member, IEEE

Abstract—Powered exoskeletons need actuators that can generate substantial assistive torque and orthoses that can efficiently transfer the assistive torque to the user. Powered exoskeletons also need to be lightweight and ergonomic to minimize the negative effects wearing the exoskeleton has on the user's effort and comfort. Here we present the design, development, and validation of an autonomous powered hip exoskeleton with high torque density. The exoskeleton actuator is based on a four-bar mechanism with integrated composite springs. A compact carbon fiber frame encloses the custom actuator, doubling as the exoskeleton thigh linkage. A self-aligning mechanism is used to avoid uncomfortable spurious forces and torques on the user's limb. Custom pelvis and thigh braces are developed using composite materials to reduce weight. A custom embedded electronic system is integrated into the pelvis brace to minimize the device weight and electrical consumption. Experiments show that the proposed powered hip exoskeleton can produce high nominal torque (41.9 Nm repetitive peak torque), high backdrivability (0.16 Nm back-driving torque), high bandwidth (23.8 Hz), and high control accuracy (2.1% steady-state error). Human tests show that the proposed exoskeleton can assist in walking, running, and stairs climbing.

Index Terms—Biomimetic and bioinspired robotics, design/control, legged locomotion, prosthetics, robotics, soft/compliant actuators.

I. INTRODUCTION

FUNDAMENTAL tradeoff exists between the mass of a powered exoskeleton and the assistance it can provide to the user. Experiments suggest that an exoskeleton's mass

Manuscript received 2 August 2021; revised 20 January 2022; accepted 1 March 2022. Date of publication 6 April 2022; date of current version 14 December 2022. Recommended by Technical Editor H. Xie and Senior Editor W. J. C. Zhang. This work was supported in part by the U.S. Department of Defense under Grant W81XWH-16-1-0701, and in part by the National Science Foundation under Grant 2046287. (Corresponding author: Tommaso Lenzi.)

The authors are with the Department of Mechanical Engineering and the Robotics Center, University of Utah, Salt Lake City, UT 84112 USA (e-mail: marshall.ishmael@utah.edu; dante.archangeli@utah.edu; t.lenzi@utah.edu).

This work involved human subjects or animals in its research. Approval of all ethical and experimental procedures and protocols was granted by University of Utah IRB Application No.: IRB_00099066 Declaration of Helsinki.

This article has supplementary material provided by the authors and color versions of one or more figures available at https://doi.org/10.1109/TMECH.2022.3159506.

Digital Object Identifier 10.1109/TMECH.2022.3159506

should be minimized and located proximally to the trunk [1]. Moreover, previous articles suggest that increasing exoskeleton assistive torque may improve metabolic results [2]. Thus, exoskeletons should be designed to maximize the assistive torque while minimizing its mass, therefore maximizing torque density. However, it is not obvious how to achieve this goal because simply increasing the assistive torque by using larger actuators results in heavier exoskeletons.

Both the mass and the maximum assistance of an exoskeleton largely depend on the exoskeleton actuator [3]. Researchers have proposed using custom motors and gearboxes with a relatively low transmission ratio [4]–[9]. These actuators are typically compact, lightweight, and quiet, but can only provide a relatively low torque (i.e., 12–20 Nm). Although higher peak torque can be obtained using this design solution, it typically comes at the cost of a substantial increase in mass [10]. To achieve higher maximum torque (e.g., 30-90 Nm) without worsening output impedance, researchers have used elastic elements in series to a geared motor with higher transmission ratios [11]–[18]. Series elastic actuators (SEAs) can achieve remarkable efficiency and mechanical power output [19]. By reducing the actuator impedance, SEAs can improve intrinsic safety. Additionally, they can serve as reliable and precise torque sensors. However, SEAs require additional actuation and sensing components, often resulting in heavier powered exoskeletons. Thus, powered exoskeletons with elastic elements do not necessarily achieve higher torque density than powered exoskeletons without elastic elements.

To mitigate the negative effect of the actuator mass, researchers have proposed locating the exoskeleton actuators closer to the trunk [20]–[22]. However, this solution requires additional transmission elements, such as Bowden cables or parallelograms, to transfer the assistance from the actuators to the user's joints. Thus, locating the actuators to the trunk typically comes at the cost of added mass and reduced efficiency. As a result, exoskeletons with actuators located on the user's trunk do not necessarily provide better outcomes than exoskeletons with actuators located on the user's legs [23].

Reducing the weight of the braces and orthosis can improve the torque density of a powered exoskeleton. However, using small braces with limited contact areas may result in increased pressure on the user's skin, reducing comfort. Moreover, lightweight braces and orthoses may flex under load, causing misalignments between the anatomical joint axis and the powered joint axis, which results in spurious forces and

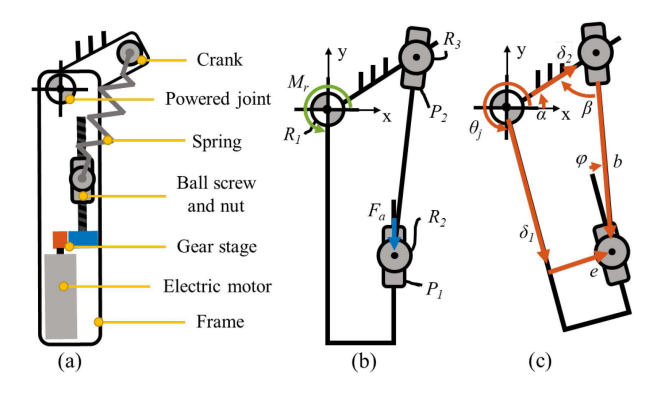


Fig. 1. High-level schematic and kinematic model of the proposed five-bar mechanism. (a) Labels main components of the actuator. The crank is grounded. (b) Outlines the five-bar mechanism $R_1\,R_2\,P_1\,R_3\,P_2$ which can be simplified to a four-bar mechanism $R_1\,R_2\,P_1\,R_3$ when P_2 is fixed. The applied force F_a produces a resultant joint moment M_r creating the powered joint R_1 . (c) Describes the kinematic variables of the five-bar mechanism. Arrow direction indicates positive force, moment, or displacement.

torques on the user's limb [11]. In addition, the flexibility in the brace and orthosis tend to deteriorate the ability of the powered exoskeleton to assist the user, for example, decreasing the bandwidth of the torque controller. Mass minimization should not come at the expenses of comfort and effectiveness.

In this article, we present the design, development, and validation of an autonomous, bilateral powered hip exoskeleton with high torque density for walking, running, and stair ascent. The contribution of this article includes three key innovations enabling this exoskeleton. The first is a high-torque actuator based on a nonlinear kinematic design with embedded composite spring. The second is lightweight, comfortable orthoses/braces with integrated self-aligning mechanisms. The third is an assistive control system that is robust to different ambulation tasks. This contribution is demonstrated by human tests showing that the proposed exoskeleton achieves the highest torque density in the field— \sim 60% higher than previously possible with matching battery weight [21].

II. MODELING

A. Kinetostatic Analysis

The proposed actuation system is based on a nonlinear kinematics with an integrated elastic element [Fig. 1(a)–(c)]. The system uses a closed kinematic chain $(R_1R_3P_2R_2P_1)$ to translate an input force F_a applied to the prismatic joint, P_1 , into an output torque M_r at the revolute joint, R_1 [Fig. 1(b)]. The prismatic input joint P_1 is powered by a linear actuator comprising a dc motor, a primary gear transmission, and a ball screw [Fig. 1(a)]. A tension/compression spring passively actuates the prismatic joint P_2 [Fig. 1(b)]. Using the notation shown in Fig. 1(c), we can derive the transmission ratio TR_1 between the input force F_a and the output torque M_r

$$T R_{1} = \frac{M_{r}}{F_{a}} = -\delta_{2} s_{\theta_{j}-\alpha} - \frac{\left(\delta_{2} c_{\theta_{j}-\alpha}\right) \left(\delta_{2} s_{\theta_{j}-\alpha} + e\right)}{\sqrt{b^{2} - \left(\delta_{2} s_{\theta_{j}-\alpha} + e\right)^{2}}}$$
 (1)

where s and c indicate sine and cosine, respectively.

In the proposed actuation system, the distance b between the revolute joints R_3 and R_2 is equivalent to the effective length of the spring (Fig. 1). Thus, the segment b is not fixed but depends on whether the spring is compressed or extended, and thus

$$b = b_o + \Delta b = b_0 - \frac{F_s}{k}.$$
 (2)

As shown in (2), the effective length of the spring b is equivalent to the sum of its resting length b_o and its deflection Δb . Moreover, the spring deflection Δb depends on the internal spring force F_s and the spring stiffness k. Finally, the spring force F_s depends on the input force F_a or the output torque M_r

$$F_s = -\frac{F_a}{c_{\wp}} = -\frac{M_r}{\delta_2 s_{\beta}}. (3)$$

By combining (1)–(3), we can obtain the transmission ratio of the proposed actuation system TR_1 as a function of the output position θ_i and the output torque M_r

$$T R_{1} = -\delta_{2} s_{\theta_{j}-\alpha} - \frac{\left(\delta_{2} c_{\theta_{j}-\alpha}\right) \left(\delta_{2} s_{\theta_{j}-\alpha} + e\right)}{\sqrt{\left(b_{o} + \frac{M_{r}}{K \delta_{2} s_{\beta}}\right)^{2} - \left(\delta_{2} s_{\theta_{j}-\alpha} + e\right)^{2}}}.$$
(4)

This analysis shows that given the dimensions of the linkages and the rest length and stiffness of the spring, we can calculate the transmission ratio of the proposed nonlinear SEA as a function of the output position θ_j and the output torque M_r . Once we know the transmission ratio TR_1 , we can calculate the input force F_a required to obtain a desired torque at the output joint. Finally, we can calculate the desired motor torque $\tau_{m,\text{static}}$ by combining the transmission ratios of the nonlinear kinematics TR_1 , the primary gear transmission TR_{gear} , and the ball screw TR_{screw}

$$\tau_{m, \text{ static}} = \frac{M_r}{\text{TR}_1 \text{ TR}_{\text{gear}} \text{TR}_{\text{screw}}}.$$
(5)

Moreover, once the deformation of the spring is known, we can find the position δ_1 of the input joint as a function of the output joint angle and torque using the kinematic model of the nonlinear actuation system

$$\delta_1 = \delta_2 c_{\theta_j - \alpha} + \sqrt{\left(b_o + \frac{M_r}{K \delta_2 s_\beta}\right)^2 - \left(\delta_2 s_{\theta_j - \alpha} + e\right)^2}. \quad (6)$$

Based on the position of the input, we can then find the velocity of the motor

$$\dot{\theta}_m = \mathrm{TR}_{\mathrm{gear}} \, \mathrm{TR}_{\mathrm{screw}} \dot{\delta}_1.$$
 (7)

As shown in (7), the motor speed $\dot{\theta}_m$ is proportional to the velocity of the prismatic input joint $\dot{\delta}_1$, multiplied by the transmission ratios of the primary gear stage (TR_{gear}) and of the ballscrew (TR_{screw}). This analysis shows that the kinetostatic model of the proposed nonlinear SEA can be used to estimate the motor torque and velocity necessary to obtain desired output position, velocity, and torque, although it does not include the effects of the actuator dynamics.

B. Dynamic Simulation Framework

Similar to our previous article [24]–[27], we used a dynamic simulation framework to guide the design of the proposed actuation system. The simulation framework captures the dynamic behavior of the proposed nonlinear elastic transmission system by integrating an electromechanical model of the linear actuator driving the input joint P_1 with the kinetostatic analysis shown in Section II-A. The simulation framework takes as input the desired torque, position, and velocity of the output joint, derived from walking, running, and stair climbing datasets [28], [29]. Based on these inputs, the framework calculates motor torque and velocity for a specific parameter set describing the dimensions of the linkages, the rest length, and stiffness of the spring.

As commonly done in the field [27], [30], [31], the dynamic model accounts for the dynamics of the linear actuator by modeling the inertial torque due to motor (H_m) and the transmission system (H_{TR}) . We also account for the friction in the linear actuator using an efficiency term $\eta_{\text{mechanics}}$. Using the motor torque (5) and the numerical derivative of the motor speed (7), we calculate the motor current as follows:

$$i_m = \frac{1}{k_t} \left(\frac{\tau_{m, \text{ static}}}{\eta_{\text{mechanics}}} + \ddot{\theta}_m \left(H_m + \frac{H_{\text{TR}}}{\text{TR}_{\text{gear}}^2} \right) \right).$$
 (8)

Once the motor current is known, the motor voltage can be calculated using

$$V_m = i_m R_m + k_v \dot{\theta}_m \tag{9}$$

where k_v is the back-EMF constant and R_m is the electrical resistance of the motor windings. The effect of inductance is neglected. After the motor voltage and current are calculated, the simulation framework checks that two basic conditions are satisfied

$$(i_{\text{mot}}^{\text{rms}} < i_{\text{nom}}) \& (|V_m| < \eta_{\text{driver}} V_s).$$
 (10)

The first condition in (10) is that the motor nominal current must be greater than the root mean square (rms) of the motor current calculated over a gait cycle for all possible activities. This condition ensures that the motor can provide the required assistance indefinitely, without overheating. The second condition is that the maximum voltage available at the motor windings must be greater than the required motor voltage when the back electromotive voltage is considered. Finally, the simulation framework provides an estimate of the electrical energy consumption. Using the dynamic simulation framework, we can explore the design space to understand the effect of the different actuation components on performance.

III. DESIGN

A. Simulations

The design of the exoskeleton followed an iterative process in which the simulation framework was used to estimate the actuation performance and to approximate the actuator size. Based on this iterative process, we selected the key actuator parameters such as the dimensions of the linkages, the stiffness of the spring,

TABLE I
DESIGN PARAMETERS OF THE PROPOSED EXOSKELETON

Parameter	Value		
V_s	28.8 V		
k_t	13.5 mNmA ⁻¹		
R	$0.341~\Omega$		
I_{nom}	5.86 A		
H_m	10.59 gcm^2		
H_{tr}	$9.55~\mathrm{gcm}^2$		
$\eta_{mechanics}$	95%		
$\eta_{ extit{driver}}$	95%		
r	43.25 mm		
α	25.5°		
B_o	90.5 mm		
k	500 N/mm		
e	11.5 mm		
TR_{screw}	3.14 rad/mm		
TR_{gear}	2.5		

and the electrical motor. The final actuation parameters of the proposed exoskeleton are listed in Table I.

The simulations show that the effects of the spring stiffness on the motor speed torque are nontrivial (Fig. 2). As expected from an SEA, the spring stiffness has a considerable effect on the motor speed [32]. Also, as predicted by the kinetostatic model (4) and (5), the spring stiffness affects the motor torque. This effect is due to the deformation of the spring causing a change in the torque ratio due to the proposed nonlinear actuator kinematics (Fig. 1), which is not common in SEAs. Compared to the stiff spring, simulations suggest that the 500 N/mm spring provides modest but consistent improvements in energy consumption per stride, peak motor torque, and peak motor speed across the three ambulation tasks. Even still, the 100 N/mm spring provides larger improvements in walking and running, while considerably increasing the peak motor speed in stair ascent. Thus, an appropriately selected spring can reduce both motor speed and torque below that of a stiff actuator (infinite stiffness case). However, there are tradeoffs that need to be considered when multiple ambulation tasks are accounted for.

With the selected parameters (Table I), the dynamic simulations predict that the proposed actuator can provide at least 50% of physiological torque assistance for 95th percentile male performing level-ground walking at stride time of 1.11 s. Furthermore, the design can provide 29% and 105% of physiologic torque assistance for a 95th percentile male performing level-ground running (stride time 0.729 s) and stair ascent (stride time 1.41 s), respectively. Thus, the actuator is expected to provide repetitive peak extension torques equal to 51, 40, and 71 Nm for walk, run, and stair ascent. The corresponding nominal (rms) current for these tasks is 5.86, 5.85, and 5.84 A.

B. Mechanics

The exoskeleton is designed using the parameters shown in Table I. The exoskeleton is powered by a custom linear actuator (Fig. 3) comprising a brushless dc motor (EC-4pole 22, 24 V,

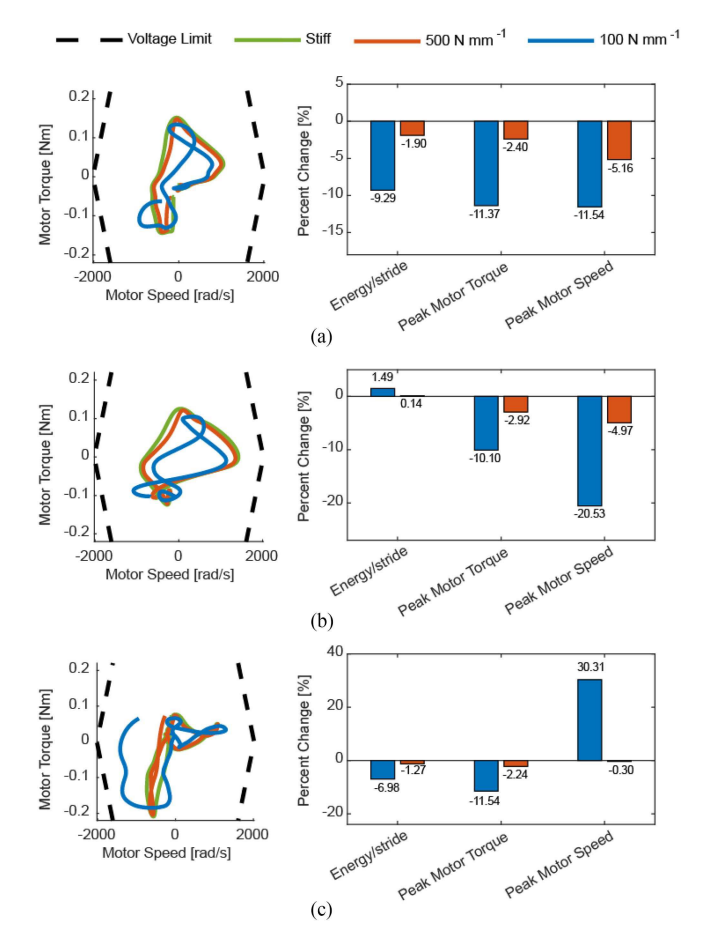


Fig. 2. Motor performance for various spring stiffness across three ambulation tasks: (a) walking, (b) running, and (c) stairs ascent. Bar plots compare performance relative to the stiff spring system.

120 W, Maxon Motors), a primary helical gear transmission (Boston Gears, 2.5:1), and a high-efficiency ball screw (6×2 , Eichenberger). A linear guide (SSELBZ8, Misumi) supports the perpendicular load on the ball screw nut. Two angular contact ball bearings support radial and axial loads, respectively, on the helical gears, similar to [25]. The linear actuator is connected to a custom-machined hip joint crank linkage (Fig. 4) through a composite three-dimensional (3-D)-printed compliant bar (Onyx with Fiberglass CFF). The composite springs can absorb 1.5 J energy at a stiffness of 500 N/mm. Dry bushings (PTFE with steel shell) support the load at the actuated hip joint. The actuator is fully enclosed by a carbon fiber frame (34 cm \times 2.9 cm \times 4.1 cm).

An active cooling system provides forced heat convection. This system consists of a fan (25-mm, Sunon Fans) located at distal end of the carbon fiber frame [Fig. 3(a)], which directs the air flow through the motor, and a fan speed control implemented in the embedded system. The fan produces a maximum of 3.0 CFM airflow at 5 VDC and 23 dB at 1 m. The fan speed changes based on rms of the motor current, dissipating heat proportionally to the motor Joule heating.

The pelvis brace comprises two sets of stiff connecting bars that merge posteriorly into a structural lumbar support, which double as housing for the battery [Fig. 3(c)]. The connecting bars

and lumbar support are fabricated using composite 3-D-printing with continuous carbon fiber filament to achieve high stiffness and low weight. Together, the connecting bars and lumbar support provide high torsional stiffness as needed to transfer the assistance to the user. The lumbar support is designed to conform to the user's lower back anatomy while allowing for a large area of contact with the user as needed to maximize comfort [Fig. 3(c)]. The box containing the embedded electronics also connects to the lumbar support. The pelvis frame connects to each of the exoskeleton thigh segment (i.e., the carbon fiber frame) with two revolute passive degrees of freedom [Fig. 4(a)] allowing for unconstrained hip abduction/adduction during ambulation [33]. Moreover, the pelvis frame connects to two flexible 3-D-printed orthoses made of thermoplastic polyurethane, which sit on the user's pelvis. The two flexible orthoses are connected anteriorly with two BOA straps, and posteriorly with one single BOA strap.

Each thigh brace comprises a stiff 3-D-printed frame located anteriorly to the user's thigh and a flexible cuff that wraps around the user's thigh [Figs. 3(c) and 4(b)]. A posterior BOA lace system allows adjusting the flexible cuff to the user's thigh. The stiff thigh frame connects to the exoskeleton thigh segments (i.e., the carbon fiber frame) through a self-aligning mechanism [Fig. 4(b)], similar to [11]. The self-aligning mechanism comprises a prismatic passive degree of freedom (SSEBL6, Misumi), and a revolute passive degree of freedom. The self-aligning mechanism minimizes the spurious forces and torques, improving user's comfort and performance [34]. A video of the device is available in the supplementary materials.

C. Embedded Sensing and Power Electronics

An overview of the electrical system of the powered hip exoskeleton is shown in Fig. 5(a). The exoskeleton power supply is a 1200 mAh, eight-cell lithium-ion battery. A 5-V regulator and a 3.3-V regulator are used to scale the supply voltage as required to power the embedded computer, the analog sensors, and the microcontroller. The motherboard includes a 32-bit microcontroller (PIC32, Microchip Technology, Inc.) and a single-board computer (RPi 3 module, Raspberry Pi Foundation).

All time-critical routines run at 1 kHz on the PIC32. The PIC32 uses pulsewidth modulation to communicate to the two motor servo drives (ESCON 50/5 Module, Maxon Motors, CH), which run the closed-loop motor current control at 50 kHz. The PIC32 uses dedicated serial peripheral interface busses to communicate with the embedded sensors and the RPi3 module, which runs the high-level control loops and data saving at 500 Hz. The RPi3 module communicates with a laptop computer using Wi-Fi. The laptop runs a graphical user interface (GUI) for data monitoring and parameter-selection purposes. Using the GUI, the experimenter can modify all the high-level control parameters while the device is operating. The PIC32, RPi module, motor servo drives, and voltage regulators are integrated on a custom motherboard as shown in Fig. 5(b). The electrical power consumption is 3.6 W with Wi-Fi ON.

A 14-bit magnetic absolute encoder board (AS5047U, AMS, USA) measures the powered hip flexion/extension angle. An inertial measurement unit (IMU, BMX160, Bosch, USA) board



Fig. 3. Powered exoskeleton comprises a hip actuator (a), a pelvis interface, and a thigh interface (b) and (c). The actuator (a) is five-bar linkage based on an offset slider crank. The pelvis interface integrates the electronics and batteries into a rigid frame that connects to the user through compliant straps and flexible 3-D-printed orthosis. The thigh interface includes a self-aligning mechanism, an anterior stiff 3-D-printed frame, and a flexible wrap-around cuff with a posterior BOA closure.

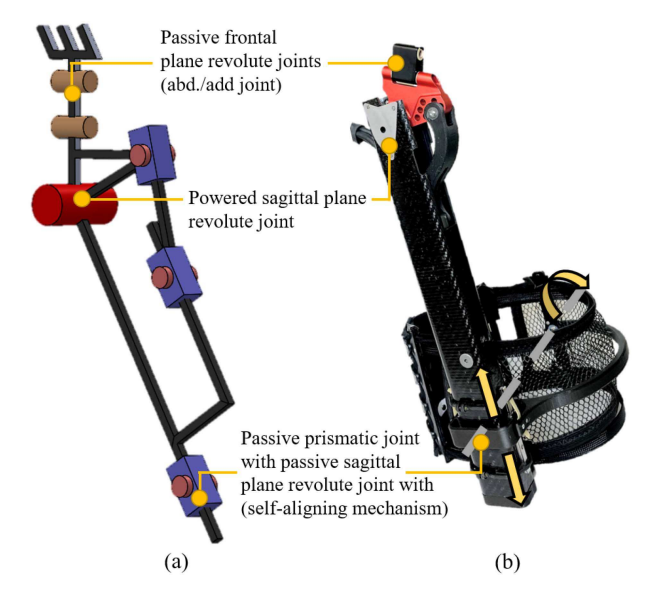


Fig. 4. Kinematic model (a) and realization of the proposed design (b). Abduction/adduction DOF is constructed of dry bushings and steel shafts while the self-aligning mechanism made of a linear guide and dry bushings.

measures the accelerations and rotational speeds and is located at the distal end of the carbon fiber frame. An incremental encoder (RM08, RLS, Slovenia) is used to measure the position of the motor shaft. Hall sensors embedded in the motor are used for commutation by the servo drives. The incremental encoder is used to estimate the position of the prismatic joint P_1 . The spring deflection is estimated by combining the position of the joints P_1 and R_1 based on the actuation kinematics. Power and data lines are separated into three shielded cables connecting the motherboard to each actuator.

TABLE II
RESULTS OF THE THERMAL EXPERIMENTS

Setup	Thermal Resistance [K/W]	Thermal Time Constant [sec]	Max Continuous Current [A]	Change from Nominal [%]
Nominal	10.7	936	4.21	-
Outside Frame	10.1	896	4.33	3.00
Inside Frame, No Fan	10.9	1241	4.17	-0.88
Inside Frame, With Fan	5.51	631	5.86	39.38

D. Weight Breakdown

The total mass of the exoskeleton is 2702 g (Table II). Each actuator weighs 567 g, making up 21% of the total weight. The passive abduction/adduction joints and the self-aligning mechanisms weigh 138 g (69 g per side or 2.5% of the total weight). The orthoses and braces weigh 894 g, corresponding to 33% of the total weight. Finally, the electrical system weighs 536–148 g for cables and connectors—making up 20% of the total weight. Notably, except for the weight of the thigh orthosis/braces (106 g per side), the whole mass of the exoskeleton is suspended from the user's trunk through the pelvis orthosis. This result is due to the passive prismatic joint of the self-aligning mechanism (Fig. 4).

IV. CONTROL

A hierarchical controller provides synchronous assistance during ambulation. At the high level, two adaptive frequency oscillators, one for each leg, estimate the gait cadence independently [35]–[37] (high level, Fig. 6). Similar to previous

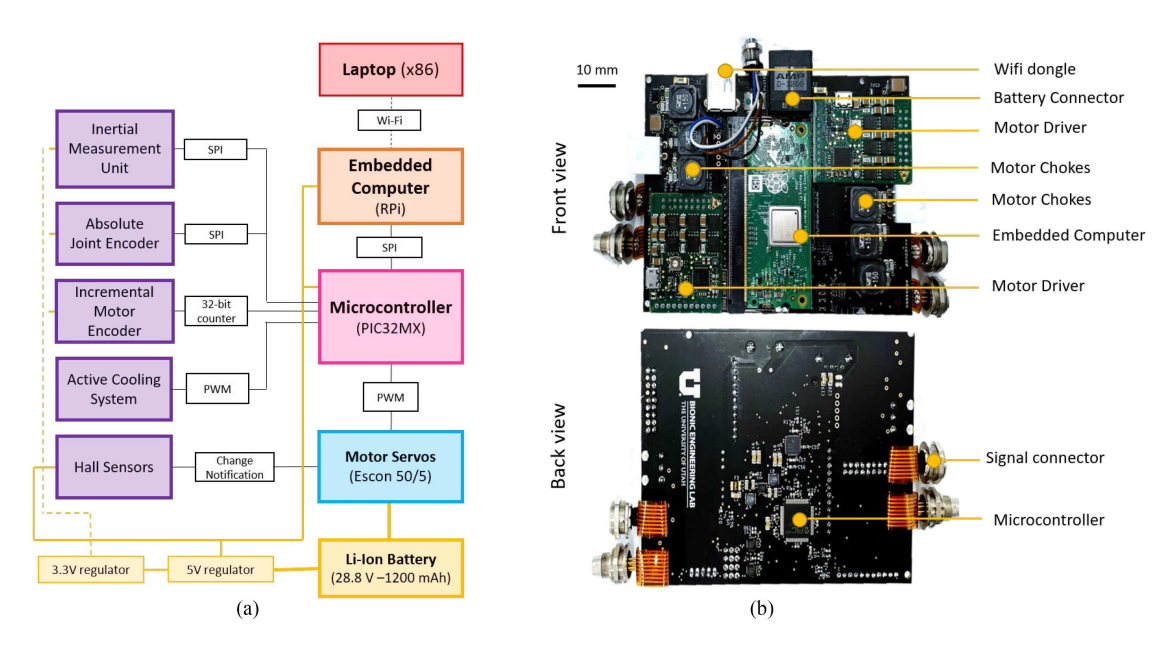


Fig. 5. (a) Conceptual electronic architecture, including computational, sensory, and power components. (b) Physical embedded electronic implementation.

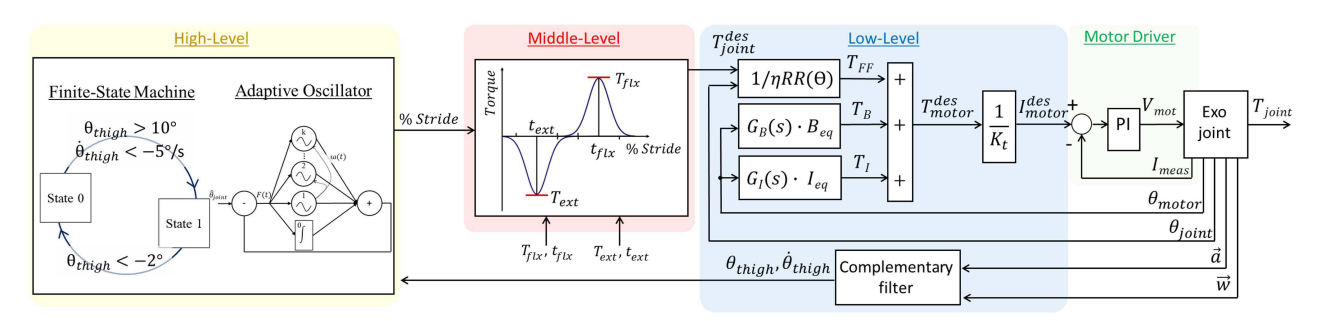


Fig. 6. Hip exoskeleton control architecture, highlighting the different control levels from high-level down to the low-level motor control.

articles [36], [38]–[40], estimation of the cadence is combined with information about the start of the gait cycle to provide a continuous estimate of the gait cycle evolution (i.e., % Stride).

Previous articles have demonstrated several methods to signal the start of the gait cycle. These methods include using foot switches [36], combing position and acceleration data [40], [41], or using peak of hip movement [20], [21]. We use the peak of the hip flexion angle (high level, Fig. 6), which is detected with a finite-state machine with two states, State 0 and State 1. The finite-state machine takes as input the thigh angular orientation and velocity in the sagittal plane (θ_{thigh}). These thigh variables are estimated online by a complementary filter combining the accelerometer (low level, \vec{a}) and gyroscope (low level, \vec{w}) data from the onboard IMU. The finite-state machine transitions from State 0 to State 1 when the thigh orientation (θ_{thigh}) is higher than 10° (i.e., the hip joint is flexed) and the thigh velocity is $(\dot{\theta}_{thigh})$ lower than -5° /s (i.e., the thigh is extending). This transition indicates that the peak of hip flexion angle has been detected, triggering the start of the gait cycle (i.e., %Stride = 0). The finite-state machine transitions from State 1 to State 0 when the thigh orientation (θ_{thigh}) is lower than -2° (i.e., the hip joint is extended).

The middle-level controller defines the desired assistive torque $(T_{\rm joint}^{\rm des})$ based on the online gait phase estimate (i.e., %Stride) received from the high-level controller. The desired assistive torque is defined online using two Gaussian functions—one for flexion and one for extension (middle level, Fig. 6). Each Gaussian function has three parameters that can be adjusted by the experimenter through the GUI

$$T_{\text{joint}}^{\text{des}} = T_{\text{flx}} \ e^{-\frac{(x - t_{\text{flx}})^2}{2\Omega_{\text{flx}}^2}} - T_{\text{ext}} \ e^{-\frac{(x - t_{\text{ext}})^2}{2\Omega_{\text{ext}}^2}}.$$
 (11)

The first parameter is the peak of the torque (i.e., $T_{\rm flx}$ and $T_{\rm ext}$). The second parameter is the timing, or percent stride, at which the peak of the torque happens (i.e., $t_{\rm flx}$ and $t_{\rm ext}$) of the peak of torque. The third parameter is the duration of the assistance, which is adjusted by changing the width of the Gaussian functions (i.e., $\Omega_{\rm flx}$ and $\Omega_{\rm ext}$). The experimenter has the option to use different parameters for the left and right side of the powered exoskeleton or to use the same parameters. Different parameters of the middle-level controller are used for walking, running, and stair climbing.

The low-level controller converts the desired assistive torque ($T_{\rm ioint}^{\rm des}$) into a desired motor current for the servo motor ($I_{\rm motor}^{\rm des}$).



Fig. 7. Bench set up for step response. The exoskeleton crank was connected to a load cell, grounded to a rigid frame. The carbon fiber frame was braced against a rigid bracket. Free body diagrams of each system (red and blue) are shown.

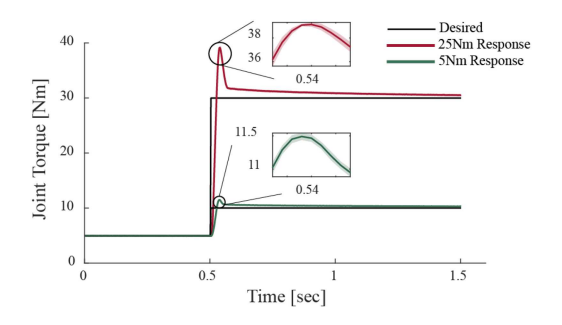


Fig. 8. Step response of the hip exoskeleton for 5 and 25 Nm desired steps. The exoskeleton was preloaded to a torque of 5 Nm before applying the step.

The low-level controller comprises a feedforward command based on the angle-dependent transmission ratio (RR(θ)). This feedforward command includes a constant factor (η) that compensates for the efficiency of the actuation system. In addition, two compensators $(G_B(s) \cdot B_{eq}, G_I(s) \cdot B_I)$ are implemented to modify the dynamic effects of the transmission system on the output torque (T_{joint}) . The compensators increase fidelity and reduce the apparent impedance at the output joint [26]. As can be seen in Fig. 6, both compensators take as input the motor position measured by the incremental encoder. The first compensator generates an online estimate of the viscous torque due to the linear velocity of the actuator. The second compensator computes a scaled and low-pass-filtered estimate of the transmission inertia similar to that presented in [42]. The coefficients of both compensators were determined experimentally with bench-top testing. These coefficients are kept constant and not expected to change. The desired current $(I_{\text{motor}}^{\text{des}})$ is calculated by first adding the feedforward term to the compensators' output and then dividing by the torque constant of the motor (K_t) .

V. BENCHTOP TESTING

To evaluate the exoskeleton torque performance, the crank of the device was rigidly attached to a six-axis load cell (Sunrise Instruments, M3713D), while the carbon fiber frame rested against an aluminum fixture (Fig. 7). The angle of the joint was 0°. Torque steps were commanded from a starting torque of 5 Nm (Fig. 8). Forces and torques at the load cell were reflected to the powered exoskeleton joint center

$$M_{\rm joint} = \vec{r}_{\rm joint,sensor} \times \vec{F}_{\rm sensor} + M_{\rm sensor}.$$
 (12)

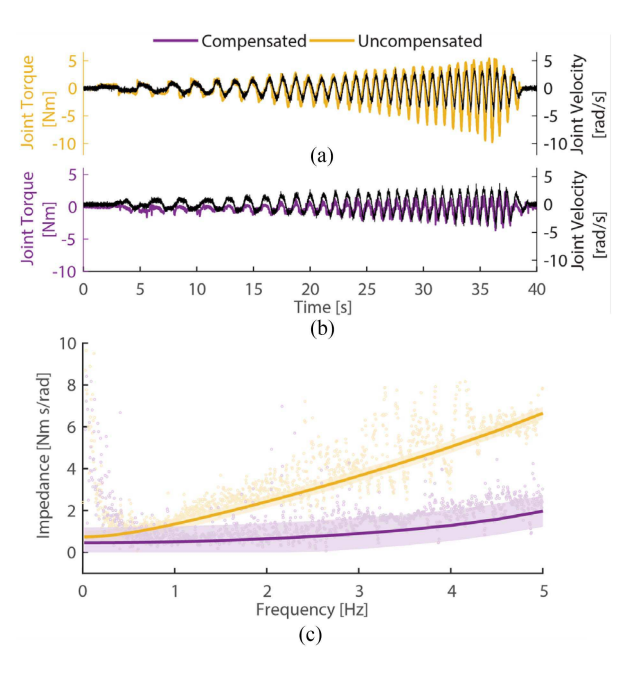


Fig. 9. (a) Uncompensated and (b) compensated manual backdriving tests. (c) Impedance of the uncompensated and compensated hip exoskeleton. Raw data points are shown as dots, and two-pole one-zero models are shown fitted to the data, and 95% confidence intervals of the model estimates are shown in the shaded region around the models.

Each step was conducted nine times. The mean and standard deviation of the measured torque at the joint center for each of the different step responses are shown in Fig. 8. The rise times were 14.5 \pm 0.2 and 14.0 \pm 0.1 ms for the 5 and 25 Nm steps, respectively. Mean rise times correspond to an estimated -3-dB bandwidth of 23.8 and 25.1 Hz for steps of 5 and 25 Nm, respectively. Percent overshoot was 29.9 \pm 1.1% and 36.7 \pm 0.6% for the 5 and 25 Nm steps, respectively. Steady-state error was 6.09 \pm 0.9% and 2.07 \pm 0.8% for the 5 and 25 Nm steps, respectively.

The output impedance of the actuator was estimated by constraining the crank of the exoskeleton to a six-axis load cell and backdriving the joint manually. Forces and torques measured by the load cell were used to calculate the exoskeleton output joint torque [Fig. 9(a) and (b)]. Static friction torque was 0.23 Nm and compensated backdriving torque was 0.16 Nm. The output impedance was estimated in the frequency domain using a two-pole one-zero model [Fig. 9(c)]. The reflected damping was 0.74 and 0.46 Nms/rad for the uncompensated and compensated system, respectively. The reflected inertia was 1.05 and 0.24 kgm² for the uncompensated and compensated system, respectively. Thus, active control decreased the reflected output joint damping and inertia by 38.3 and 77.8%, respectively.

A thermal analysis was conducted to assess the behavior of the active cooling system. To this end, we commanded 4 A of continuous motor current for 1 h while the temperature of the motor housing was recorded using a thermocouple. The test was repeated in three configurations: (1) the assembled motor and actuation system outside of the carbon fiber housing, (2) the assembled motor and actuation system inside the carbon fiber

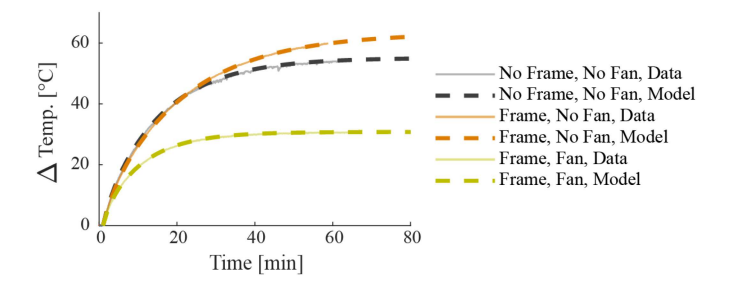


Fig. 10. Thermal response to a 4 A step input of current. The step responses were fit by a second-order system shown by the dashed lines $(R^2 > 0.999 \text{ for all fits})$.

frame with the active cooling system powered OFF, and (3) the assembled motor and actuation system inside the carbon fiber frame with the active cooling system powered ON. For each configuration, we calculated the thermal resistance, time constant, and the maximum continuous current using a second-order model as done in our previous article [24].

The results of the thermal analysis are shown in Fig. 10 and Table II. The coefficients of determination for the thermal model were $R^2>0.999$ for all tested configurations. The thermal constants estimated for the actuation system outside the frame were comparable to the nominal values provided by the motor manufacturer (i.e., 3% difference in nominal current). When placed inside the frame with the active cooling system OFF, there was a small worsening of the thermal dissipation (i.e., $\sim 1\%$ difference in nominal current). Most importantly, using the active cooling system decreases the thermal resistance substantially, increasing the maximum continuous current to 5.86 A, which is a 39% improvement compared to the nominal value.

VI. HUMAN EXPERIMENTS

The performance of the proposed hip exoskeleton was tested with three healthy subjects (26 \pm 3 years old, 181 \pm 3 cm, and 80 ± 19 kg). The subjects were given 30 min to familiarize with the powered hip exoskeleton and the related control algorithm prior to data recording. During the familiarization period, an experimenter tuned the assistive controller. The subjects were asked to walk on a treadmill at 1.2 m/s, run on a treadmill at 2.2 m/s, and ascend an ADA-compliant staircase comprising 10 steps at their preferred cadence. The goal of the experiment was to quantify the maximum assistive torque that the exoskeleton can provide during ambulation. To this end, for each ambulation task, the experimenter increased the desired exoskeleton torque while the users ambulated with the exoskeleton until the measured torque reached a limit over which it stopped increasing. The experimental protocol was approved by the University of Utah Institutional Review Board. Written informed consent was provided by the subjects before the experiment took place. The subjects consented to disseminate pictures and videos of the experiments.

Gait phase evolution was estimated by the exoskeleton using an adaptive oscillator and finite-state machine (Fig. 6). While walking, gait phase estimation averaged 0.992 at stride reset. While ascending stairs, gait phase estimation averaged 0.993 at

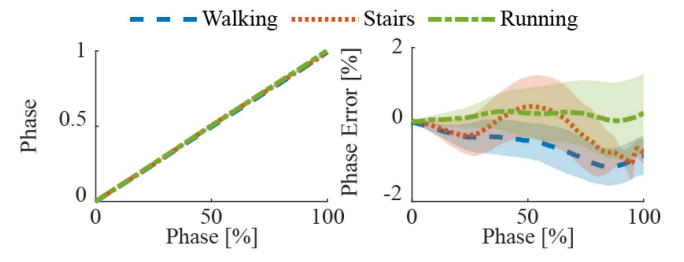


Fig. 11. Finite-state machine and adaptive oscillator allow assisting walking, running, and stair climbing without changing the parameters.

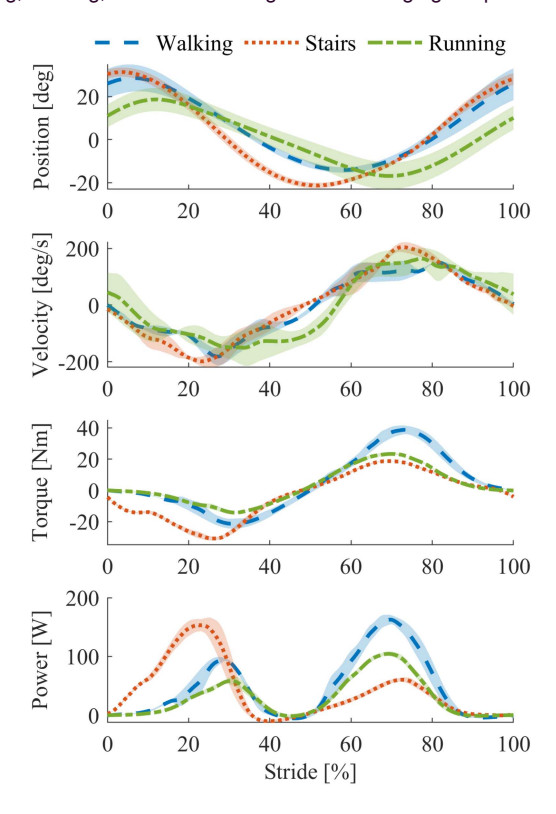


Fig. 12. Results measured from the exoskeleton during different ambulation activities. Estimated signals are shown in red with the standard deviation shaded around the average.

reset, and during running the average was 1.00 at reset (Fig. 11). Qualitatively, the worst phase error at stride reset across all subjects and tasks was less than 2% (Fig. 11).

During walking, the subjects received 41.9 Nm peak flexion assistance on average per stride (Fig. 12). The maximum value of peak flexion assistance estimated from the exoskeleton during walking was 47.3 Nm. Similar to walking, peak assistance during running occurred during flexion. Flexion assistance peaked on average at 24.5 Nm (Fig. 12) and achieved a highest maximum at 30.0 Nm. Peak assistance during stairs ascent occurred during extension of the hip. Peak extension torque while ascending stairs was on average –33.1 Nm (Fig. 12), but the maximum recorded assistance level was –38.2 Nm. Peak power was positive for all activities. The positive power peaked on average at 175.5 and 112.4 W, for walking and running, respectively. During stair ascent, peak power was on average 183.7 W. Based on the results of the human studies, we computed the actuator torque density (73.9 Nm/kg) and our powered hip exoskeleton

TABLE III
EXOSKELETON WEIGHT BREAKDOWN

System	Mass (g)		
Motor and encoder Transmission and four bar components Carbon fiber frame and main joint	156 x 2 293 x 2 118 x 2	Actuator 567 x 2	
Abduction passive DOF Thigh passive DOF	25 x2 44x 2	Passive DOFs 69 x 2	
Pelvis orthosis Thigh orthosis	682 x1 106 x 2	Orthoses/braces 894 x1	
Electronics boards Battery Power and data cables Case and Fans	Battery 204 x1 Electrical r and data cables 74×2 536×1		
Bilateral exoskeleton	2702		

torque density (15.5 Nm/kg). Table IV provides a comparative analysis of existing powered hip exoskeletons focusing on the exoskeleton and actuator torque density during ambulation.

VII. DISCUSSION

Our comparative analysis (Table IV) shows the exoskeleton torque density calculated as the average peak of the assistance measured during ambulation divided by total mass of the exoskeleton. The average peak torque recorded during ambulation depends not only on the maximum torque capabilities of the exoskeleton actuator but also on the ability of the exoskeleton braces/orthoses to effectively transfer the torque to the user. Moreover, the calculated exoskeleton torque density considers the mass of the interfaces and other essential components such as the battery and the electrical system. To maximize the exoskeleton torque density during ambulation, we propose a holistic design approach that combines high-performance electromechanical actuators (i.e., linear actuator), composite materials (i.e., machined carbon-fiber thigh frame, 3-D printed composite actuator linkages, and carbon-composite pelvis orthosis and frame), and custom embedded electronics (i.e., PIC32, RPi module, and embedded servodrives). The powered hip exoskeleton presented in this article demonstrates this design approach.

High torque density is achieved by maximizing torque and minimizing mass. Our average peak torque (\sim 42 Nm) is similar to that achieved by the Harvard's soft Exosuit (Table IV). As tested in this article, our exoskeleton uses a 0.204-kg battery, which provides \sim 1-h continuous walking, weighs 2.7 kg, and achieves a torque density of 15.52 Nm/kg. If we match the battery weight used in the Harvard Exosuit (1.01 kg), the weight of our exoskeleton increases to 3.5 kg, resulting in a torque density of 11.97 Nm/kg. Thus, even after matching the battery weight, our device achieves a substantially higher torque density than the Harvard Exosuit (11.97 vs. 7.62 Nm/kg, 57% increase). Notably, our exoskeleton can provide torque both in flexion and extension, whereas the Exosuit can provide torque in extension only. The difference in torque density is mostly due to the actuators. Our exoskeleton uses a 0.567 kg actuator (73.9 Nm/kg actuator torque density). In contrast, the Exosuit uses a 1.337 kg actuator (28.5 Nm/kg actuator torque density). The lower actuator torque density in the Exosuit may be due to the low

efficiency of the Bowden cables used in their system and the low torque density of the stock planetary gearbox.

The powered hip exoskeletons built by CUNY, Honda, and Samsung have similar total weight to our powered hip exoskeleton. However, these devices produce substantially lower torque during ambulation (6–20 Nm) than our device (~42 Nm). Thus, the torque density of CUNY, Honda, and Samsung is considerably lower than that of our device (2.14–5.88 Nm/kg vs. 15.52 Nm/kg), although this analysis has some limitations. The battery weight of our device is similar to the one used by Honda [8], but CUNY and Samsung did not report the weight of their battery.

Overall, our analysis suggests that high torque dense exoskeletons tend to use torque-dense actuators, whereas exoskeletons with low torque density have multiple actuators (Panasonic), heavy interfaces (Georgia Tech), or produce low torque (Honda). The battery weight is a confounding factor, which is not often reported. To limit this issue, we calculated torque density for our device with both the lightest and heaviest battery reported (0.2–1 kg). Despite using a heavier battery, our results show that the proposed holistic design approach can achieve a substantially higher exoskeleton torque density (1.6X–11.1X) than any powered hip exoskeletons previously developed (Table IV).

Our exoskeleton uses a high-torque, low-weight actuator based on a complaint four-bar mechanism. A small fan dissipates heat, increasing the maximum continuous current and motor torque by $\sim 40\%$ (Table II). To avoid potential voltage saturation (9) and improve the transient behavior, we use a 28.8-V battery pack, which is 20% higher than the nominal motor voltage. The compliant linkages in the proposed actuator (Fig. 2) are 3-D-printed using continuous fiber glass, obtaining comparable stiffness to other exoskeletons using SEAs (\sim 500 N mm⁻¹). The lightweight carbon-fiber tube enclosing the actuator works as a structural component of the transmission system, a duct routing airflow over the motor, a protective frame for the actuator, and a means to transfer the exoskeleton assistance to the user. Thus, additional protective covers and dedicated exoskeleton thigh segments are not necessary, keeping the overall exoskeleton mass low. The proposed actuation system weighs 567 g (Table II I) and can provide an average peak torque of \sim 42 Nm during ambulation (Fig. 12), achieving a torque density of 73.9 Nm/kg (Table IV). To the best of our knowledge, this actuator torque density is the highest in the field (Table IV).

In our design, the actuation system is located directly on the thigh (Fig. 3). In contrast, in most powered hip exoskeletons, the actuator is coaxial to the user's hip joint [6], [8], [16] or remotely located on the user's back/trunk [14], [20]–[22]. Placing the exoskeleton actuation coaxial to the user's hip joint or on the trunk might interfere with arm swing during ambulation or prohibit seated posture. By locating the actuation on the lateral thigh, we were able to achieve a small frontal plane form factor (29.2-mm width). Furthermore, the compact battery and custom control electronics—41.6-mm width in the sagittal plane—rest against the lumbar region of the trunk. The resulting exoskeleton design promotes natural arm motion during ambulation and ordinary sitting positions as demonstrated in the video attachment.

			_	Measured During Ambulation		
Exoskeleton	Actuator Weight [kg]	Battery Weight [kg]	Total Weight [kg]	Average Peak Torque [Nm]	Actuator Torque Density [Nm/kg]	Exoskeleton Torque Density [Nm/kg]
Utah [this study]	0.567	0.204-1.011	2.7-3.5**	41.9	73.9	15.52-11.97**
Harvard* [21]	1.337	1.011	5.0	38.1	28.5	7.62
CUNY [4]	0.777		3.4	20	25.7	5.88
Samsung [9]			2.8	10.9		3.89
NCSU ⁺ [16][17]	1.5		9.2	34.3	22.9	3.73
ASU [18]	1.135		2.95	9	7.9	3.05
SSSA° [20]	1.2		4.2	10	8.3	2.38
Honda [8]		0.200	2.8	6		2.14
Georgia Tech [14]	1.5	1.04	7	14.1	9.4	2.01
Panasonic [#] [22]	0.58		9.3	10	17.2	1.08

TABLE IV
HIP EXOSKELETON COMPARISON

-Not reported; * extension only; offboard control and batteries; + powered abduction and adduction; # multijoint actuator ** with 1.011-kg battery as in the Harvard Exosuit [21].

In the proposed exoskeleton, the brace frames are fabricated using carbon composite 3-D-printing with continuous filament. This solution achieves a relatively high stiffness in the assisted, sagittal plane, while being quite lightweight (Table III). However, accommodating different users requires multiple size of the frame. The user's limb is suspended inside the 3-D-printed brace using adjustable orthoses (Figs. 3 and 4) [11]. The orthoses increase the area of contact with the user's limb, reducing the pressure on the user's skin, which improves comfort. Compared to the flexible, size-adjustable solution used in our earlier prototype [40], the current orthosis/brace solution allows for higher assistive torque to be effectively and comfortably transferred to the user. Thus, the proposed orthosis/brace design enables the hip exoskeleton to achieve high exoskeleton torque density during ambulation.

A lightweight self-aligning mechanism was integrated into the powered hip exoskeleton. Although this self-aligning mechanism increases the exoskeleton mass (69 g, Table III), it facilitates physiological joint movement across ambulation modes while reducing spurious forces and torques on the user's leg. Our previous article has shown that self-aligning mechanisms can significantly improve both user's comfort and performance [11], [34]. Thus, the proposed self-aligning mechanism may provide important benefits to the user at the cost of a small added mass.

Reducing the mass of the exoskeleton should not sacrifice actuation performance. Output impedance is a useful metric to assess the ability of an exoskeleton to physically interact with the user. Reducing the controlled and uncontrolled inertia and damping of an exoskeleton is fundamental to obtain low output impedance. This objective can be achieved using a low transmission ratio [4], [8], [9], [16], by slacking the actuation cables [21] or by closed-loop control [4], [14], [17]. Our actuator combines a relatively high transmission ratio (up to 360) with a low-inertia motor (8.91 gcm²), achieving an uncompensated backdriving torque of 0.23 Nm. With dynamic compensations ON, the backdriving torque was further reduced to 0.16 Nm, without closed-loop torque control. Thus, the output impedance of our actuator is comparable to [20] (0.17 Nm) and less than half that of [4], [14] (0.4 and 0.7 Nm, respectively).

Previous articles have shown the importance of torque control bandwidth for powered exoskeletons. In general, the bandwidth of an assistive exoskeleton actuator should be high enough to capture both the steady-state and the transient behavior of leg dynamics during ambulation [43], [44]. Our torque controller achieved 25 Hz bandwidth with a 25 Nm step response, which is comparable to many devices in the field.

The proposed finite-state machine was selected following pilot studies because of its robustness to different ambulation tasks, ease of tuning, and ability to work in a unilateral exoskeleton configuration [45]. Three subjects tested the exoskeleton, walking, running, and ascending stairs. The parameters of the finite-state machine and adaptive oscillators were unchanged between different ambulation tasks and subjects (Fig. 6). Experimental results show that the proposed finite-state machine can reliably detect the maximum thigh angle as needed to estimate the gait phase (Fig. 11). These results suggest that the proposed controller is robust to initial unintended misalignments and movements of the interface due to the exoskeleton torque. Further experiments are necessary to investigate the performance of the proposed assistive controller, including kinematics analysis for nonsteady-state activities such as starting/stopping and turning.

A. Limitations

The design framework and performance evaluation presented in this article are not without limitations. Our design simulations use biomechanical assistance profiles to drive motor and transmission selection. However, the Gaussian assistance profile used to evaluate the performance of the exoskeleton does not perfectly match those observed in natural biomechanics. Consequently, the motor and transmission selected might not be the best option for the given Gaussian assistance. This mismatch is due to the fact that Gaussian assistance was considered more effective than biomechanical assistance during pilot testing.

Adding a physical spring to an electromechanical actuator improves performance but it typically comes at the cost of increased complexity and weight. In our design, the spring is integrated in the four-bar mechanism, fundamentally replacing a stiff linkage

(Figs. 1 and 3). So it does not add complexity. Moreover, we used composite 3-D-printing technology, which means the spring is lighter and less expensive that the stiff linkages it replaces. However, using this manufacturing technique, we were not able to build a reliable spring more compliant than 500 N mm⁻¹ to fit within the small exoskeleton envelope, although the simulations show that a more compliant spring could substantially increase performance in walking and running. Future article could overcome this limitation using a different material or a different manufacturing technique.

Only three healthy subjects participated in the experiments to assess the performance of the proposed exoskeleton. Thus, the exoskeleton performance may not generalize to a broader population due to a variety of reasons including interface fit, assistance timing, or finite-state machine generalization.

VIII. CONCLUSION

Increasing the torque density of autonomous powered exoskeletons is fundamental to successfully translate these devices to the real world. This article contributes new actuation, physical human—robot interfaces, and control designs. Combined, these advances enable an autonomous, bilateral powered hip exoskeleton to achieve the highest torque density in the field. Using the presented kinetostatic model and a dynamic simulation framework, we apply an iterative, holistic design approach to reduce the mass, and increase the assistance of the exoskeleton. Using a hierarchical assistive controller, we can provide synchronous assistance to the exoskeleton user during walking, running, and stair climbing without need for subject—or task-specific tuning. Future article should focus on addressing the limitations of this article and on assessing the performance of the exoskeleton on more subjects.

REFERENCES

- [1] R. C. Browning, J. R. Modica, R. Kram, and A. Goswami, "The effects of adding mass to the legs on the energetics and biomechanics of walking," *Med. Sci. Sports Exercise*, vol. 39, no. 3, pp. 515–525, 2007, doi: 10.1249/mss.0b013e31802b3562.
- [2] B. T. Quinlivan et al., "Assistance magnitude versus metabolic cost reductions for a tethered multiarticular soft exosuit," Sci. Robot., vol. 2, no. 2, pp. eaah4416, Jan. 2017, doi: 10.1126/scirobotics.aah4416.
- [3] M. del C. Sanchez-Villamañan, J. Gonzalez-Vargas, D. Torricelli, J. C. Moreno, and J. L. Pons, "Compliant lower limb exoskeletons: A comprehensive review on mechanical design principles," *J. Neuroeng. Rehabil.*, vol. 16, no. 1, Dec. 2019, Art. no. 55, doi: 10.1186/s12984-019-0517-9.
- [4] S. Yu et al., "Quasi-direct drive actuation for a lightweight hip exoskeleton with high backdrivability and high bandwidth," *IEEE/ASME Trans. Mechatron.*, vol. 25, no. 4, pp. 1794–1802, Aug. 2020, doi: 10.1109/TMECH.2020.2995134.
- [5] D. Lee, B. J. Mclain, I. Kang, and A. Young, "Biomechanical comparison of assistance strategies using a bilateral robotic knee exoskeleton," *IEEE Trans. Biomed. Eng.*, vol. 68, no. 9, pp. 2870–2879, Sep. 2021, doi: 10.1109/TBME.2021.3083580.
- [6] K. Seo, J. Lee, Y. Lee, T. Ha, and Y. Shim, "Fully autonomous hip exoskeleton saves metabolic cost of walking," in *Proc. IEEE Int. Conf. Robot. Automat.*, May 2016, pp. 4628–4635, doi: 10.1109/ICRA.2016.7487663.
- [7] H. Zhu, C. Nesler, N. Divekar, V. Peddinti, and R. Gregg, "Design principles for compact, backdrivable actuation in partial-assist powered knee orthoses," *IEEE/ASME Trans. Mechatron.*, vol. 26, no. 6, pp. 3104–3115, Dec. 2021, doi: 10.1109/TMECH.2021.3053226.

- [8] C. Buesing et al., "Effects of a wearable exoskeleton stride management assist system (SMA) on spatiotemporal gait characteristics in individuals after stroke: A randomized controlled trial," J. Neuroeng. Rehabil., vol. 12, no. 1, Dec. 2015, Art. no. 69, doi: 10.1186/s12984-015-0062-0.
- [9] B. Lim, J. Jang, J. Lee, B. Choi, Y. Lee, and Y. Shim, "Delayed output feedback control for gait assistance and resistance using a robotic exoskeleton," *IEEE Robot. Autom. Lett.*, vol. 4, no. 4, pp. 3521–3528, Oct. 2019, doi: 10.1109/LRA.2019.2927937.
- [10] G. Lv, H. Zhu, and R. D. Gregg, "On the design and control of highly backdrivable lower-limb exoskeletons: A discussion of past and ongoing work," *IEEE Control Syst.*, vol. 38, no. 6, pp. 88–113, Dec. 2018, doi: 10.1109/MCS.2018.2866605.
- [11] S. V. Sarkisian, M. K. Ishmael, G. R. Hunt, and T. Lenzi, "Design, development, and validation of a self-aligning mechanism for high-torque powered knee exoskeletons," *IEEE Trans. Med. Robot. Bionics*, vol. 2, no. 2, pp. 248–259, Mar. 2020, doi: 10.1109/tmrb.2020.2981951.
- [12] M. K. Shepherd and E. J. Rouse, "Design and validation of a torque-controllable knee exoskeleton for sit-to-stand assistance," *IEEE/ASME Trans. Mechatron.*, vol. 22, no. 4, pp. 1695–1704, Apr. 2017, doi: 10.1109/TMECH.2017.2704521.
- [13] J. F. Veneman, "A series elastic- and Bowden-cable-based actuation system for use as torque actuator in exoskeleton-type robots," *Int. J. Robot. Res.*, vol. 25, no. 3, pp. 261–281, Mar. 2006, doi: 10.1177/0278364906063829.
- [14] I. Kang, H. Hsu, and A. J. Young, "Design and validation of a torque controllable hip exoskeleton for walking assistance," in *Proc.* ASME Dyn. Syst. Control Conf., Oct. 2018, pp. V001T12A002, doi: 10.1115/DSCC2018-9198.
- [15] T. Zhang and H. Huang, "Design and control of a series elastic actuator with clutch for hip exoskeleton for precise assistive magnitude and timing control and improved mechanical safety," *IEEE/ASME Trans. Mechatron.*, vol. 24, no. 5, pp. 2215–2226, Oct. 2019, doi: 10.1109/TMECH.2019.2932312.
- [16] T. Zhang, M. Tran, and H. Huang, "Design and experimental verification of hip exoskeleton with balance capacities for walking assistance," *IEEE/ASME Trans. Mechatron.*, vol. 23, no. 1, pp. 274–285, Jan. 2018, doi: 10.1109/TMECH.2018.2790358.
- [17] T. Zhang, M. Tran, and H. Huang, "Admittance shaping-based assistive control of SEA-driven robotic hip exoskeleton," *IEEE/ASME Trans. Mechatron.*, vol. 24, no. 4, pp. 1508–1519, Apr. 2020, doi: 10.1109/TMECH.2019.2916546.
- [18] T. G. Sugar, E. Fernandez, D. Kinney, K. W. Hollander, and S. Redkar, HeSA, Hip Exoskeleton for Superior Assistance, vol. 16. Cham, Switzerland: Springer, 2017, pp. 319–323.
- [19] N. Paine, S. Oh, and L. Sentis, "Design and control considerations for high performance series elastic actuators," *IEEE/ASME Trans. Mechatron.*, vol. 19, no. 99, pp. 1–12, Jun. 2013, doi: 10.1109/TMECH.2013.2270435.
- [20] F. Giovacchini et al., "A light-weight active orthosis for hip movement assistance," Robot. Auton. Syst., vol. 73, pp. 123–134, Nov. 2015, doi: 10.1016/j.robot.2014.08.015.
- [21] J. Kim *et al.*, "Reducing the metabolic rate of walking and running with a versatile, portable exosuit," *Science*, vol. 365, no. 6454, pp. 668–672, Aug. 2019, doi: 10.1126/science.aav7536.
- [22] S. W. John, K. Murakami, M. Komatsu, and S. Adachi, "Cross-wire assist suit concept, for mobile and lightweight multiple degree of freedom hip assistance," in *Proc. IEEE Int. Conf. Rehabil. Robot.*, Aug. 2017, pp. 387–393, doi: 10.1109/ICORR.2017.8009278.
- [23] G. S. Sawicki, O. N. Beck, I. Kang, and A. J. Young, "The exoskele-ton expansion: Improving walking and running economy," *J. Neuroeng. Rehabil.*, vol. 17, 2020, Art. no. 25, doi: 10.1186/s12984-020-00663-9.
- [24] T. Lenzi, M. Cempini, L. Hargrove, and T. Kuiken, "Design, development, and testing of a lightweight hybrid robotic knee prosthesis," *Int. J. Robot. Res.*, vol. 37, no. 8, pp. 953–976, Jul. 2018, doi: 10.1177/0278364918785993.
- [25] M. Tran, L. Gabert, M. Cempini, and T. Lenzi, "A lightweight, efficient fully powered knee prosthesis with actively variable transmission," *IEEE Robot. Autom. Lett.*, vol. 4, no. 2, pp. 1186–1193, Apr. 2019, doi: 10.1109/LRA.2019.2892204.
- [26] L. Gabert, S. Hood, M. Tran, M. Cempini, and T. Lenzi, "A compact, lightweight robotic ankle-foot prosthesis: Featuring a powered polycentric design," *IEEE Robot. Autom. Mag.*, vol. 27, no. 1, pp. 87–102, Mar. 2020, doi: 10.1109/MRA.2019.2955740.
- [27] T. Lenzi, M. Cempini, L. J. Hargrove, and T. A. Kuiken, "Design, development, and validation of a lightweight nonbackdrivable robotic ankle prosthesis," *IEEE/ASME Trans. Mechatron.*, vol. 24, no. 2, pp. 471–482, Apr. 2019, doi: 10.1109/TMECH.2019.2892609.

- [28] A. S. Voloshina and D. P. Ferris, "Biomechanics and energetics of running on uneven terrain," J. Exp. Biol., vol. 218, no. 5, pp. 711–719, 2015, doi: 10.1242/jeb.106518.
- [29] R. Riener, M. Rabuffetti, and C. Frigo, "Stair ascent and descent at different inclinations," *Gait Posture*, vol. 15, no. 1, pp. 32–44, Feb. 2002.
- [30] E. J. Rouse, L. M. Mooney, E. C. Martinez-Villalpando, and H. M. Herr, "Clutchable series-elastic actuator: Design of a robotic knee prosthesis for minimum energy consumption," in *Proc. IEEE Int. Conf. Rehabil. Robot.*, Jun. 2013, pp. 1–6, doi: 10.1109/ICORR.2013.6650383.
- [31] E. A. Bolivar Nieto, S. Rezazadeh, and R. D. Gregg, "Minimizing energy consumption and peak power of series elastic actuators: A convex optimization framework for elastic element design," *IEEE/ASME Trans. Mechatron.*, vol. 24, no. 3, pp. 1334–1345, Jun. 2019, doi: 10.1109/TMECH.2019.2906887.
- [32] G. A. Pratt and M. M. M. Williamson, "Series elastic actuators," in *Proc. IEEE/RSJ Int. Conf. Intell. Robots Syst. Hum. Robot Interact. Cooperative Robots*, Aug. 1995, pp. 399–406, doi: 10.1109/IROS.1995.525827.
- [33] G. Bovi, M. Rabuffetti, P. Mazzoleni, and M. Ferrarin, "A multiple-task gait analysis approach: Kinematic, kinetic and EMG reference data for healthy young and adult subjects," *Gait Posture*, vol. 33, no. 1, pp. 6–13, Jan. 2011, doi: 10.1016/j.gaitpost.2010.08.009.
- [34] S. V. Sarkisian, M. K. Ishmael, and T. Lenzi, "Self-aligning mechanism improves comfort and performance with a powered knee exoskeleton," *IEEE Trans. Neural Syst. Rehabil. Eng.*, vol. 29, pp. 629–640, Mar. 2021, doi: 10.1109/TNSRE.2021.3064463.
- [35] R. Ronsse, N. Vitiello, T. Lenzi, J. van den Kieboom, M. C. Carrozza, and A. J. Ijspeert, "Human–robot synchrony: Flexible assistance using adaptive oscillators," *IEEE Trans. Biomed. Eng.*, vol. 58, no. 4, pp. 1001–1012, Apr. 2011, doi: 10.1109/TBME.2010.2089629.
- [36] T. Lenzi, M. C. Carrozza, and S. K. Agrawal, "Powered hip exoskeletons can reduce the user's hip and ankle muscle activations during walking," *IEEE Trans. Neural Syst. Rehabil. Eng.*, vol. 21, no. 6, pp. 938–948, Jun. 2013, doi: 10.1109/TNSRE.2013.2248749.
- [37] R. Ronsse, S. M. M. De Rossi, N. Vitiello, T. Lenzi, M. C. Carrozza, and A. J. Ijspeert, "Real-time estimate of velocity and acceleration of quasiperiodic signals using adaptive oscillators," *IEEE Trans. Robot.*, vol. 29, no. 3, pp. 783–791, Jun. 2013, doi: 10.1109/TRO.2013.2240173.
- [38] R. Ronsse et al., "Oscillator-based assistance of cyclical movements: Model-based and model-free approaches," Med. Biol. Eng. Comput., vol. 49, no. 10, pp. 1173–1185, Oct. 2011, doi: 10.1007/s11517-011-0816-1.
- [39] R. Ronsse et al., "Oscillator-based walking assistance: A model-free approach," in Proc. Int. Conf. Rehabil. Robot., Jun. 2011, pp. 1–6, doi: 10.1109/ICORR.2011.5975352.
- [40] M. K. Ishmael, M. Tran, and T. Lenzi, "ExoProsthetics: Assisting above-knee amputees with a lightweight powered hip exoskeleton," in *Proc. 16th Int. Conf. Rehabil. Robot.*, Jun. 2019, pp. 925–930, doi: 10.1109/ICORR.2019.8779412.
- [41] J. Jang, K. Kim, J. Lee, B. Lim, and Y. Shim, "Assistance strategy for stair ascent with a robotic hip exoskeleton," in *Proc. IEEE/RSJ Int. Conf. Intell. Robots Syst.*, Oct. 2016, pp. 5658–5663, doi: 10.1109/IROS.2016.7759832.
- [42] G. Aguirre-Ollinger, J. E. Colgate, M. A. Peshkin, and A. Goswami, "Inertia compensation control of a one-degree-of-freedom exoskeleton for lower-limb assistance: Initial experiments," *IEEE Trans. Neu*ral Syst. Rehabil. Eng., vol. 20, no. 1, pp. 68–77, Jan. 2012, doi: 10.1109/TNSRE.2011.2176960.

- [43] K. Kong, J. Bae, and M. Tomizuka, "Control of rotary series elastic actuator for ideal force-mode actuation in human-robot interaction applications," *IEEE/ASME Trans. Mechatron.*, vol. 14, no. 1, pp. 105–118, Feb. 2009, doi: 10.1109/TMECH.2008.2004561.
- [44] D. A. Winter, Biomechanics and Motor Control of Human Movement, 2nd ed. Hoboken, NJ, USA: Wiley, 1990, Art. no. 386.
- [45] M. K. Ishmael, D. Archangeli, and T. Lenzi, "Powered hip exoskeleton improves walking economy in individuals with above-knee amputation," *Nature Med.*, vol. 27, no. 10, pp. 1783–1788, Oct. 2021, doi: 10.1038/s41591-021-01515-2.



Marshall K. Ishmael (Student Member, IEEE) received the M.S. degree in mechanical engineering from the University of Utah, Salt Lake City, UT, USA, in 2016, where he currently working toward the Ph.D. degree in mechanical engineering.

He is currently a member of the Bionic Engineering Laboratory. His research interests include mechatronic design and control assisting wearable robots.



Dante Archangeli received the B.S. degree in mechanical engineering from Yale University, New Haven, CT, USA, in 2017. He is currently working toward the Ph.D. degree in mechanical engineeringat the University of Utah, Salt Lake City, UT, USA, while working in the Bionic Engineering Laboratory.

His research interests include exoskeletons and rehabilitation robotics.



Tommaso Lenzi (Member, IEEE) received the Ph.D. degree in biorobotics from Scuola Superiore Sant'Anna, Pisa, Italy, in 2012.

He is currently an Assistant Professor with the Department of Mechanical Engineering, University of Utah, Salt Lake City, UT, USA, and a Core Faculty with the Utah Robotics Center, Salt Lake City, UT, USA.